



HAL
open science

Bioinspired polydopamine nanoparticles: synthesis, nanomechanical properties, and efficient PEGylation strategy

Islam Zmerli, Jean-Philippe Michel, Ali Makky

► **To cite this version:**

Islam Zmerli, Jean-Philippe Michel, Ali Makky. Bioinspired polydopamine nanoparticles: synthesis, nanomechanical properties, and efficient PEGylation strategy. *Journal of materials chemistry B*, 2020, 8 (20), pp.4489-4504. 10.1039/C9TB02769F . hal-04225722

HAL Id: hal-04225722

<https://hal.science/hal-04225722v1>

Submitted on 3 Oct 2023

HAL is a multi-disciplinary open access archive for the deposit and dissemination of scientific research documents, whether they are published or not. The documents may come from teaching and research institutions in France or abroad, or from public or private research centers.

L'archive ouverte pluridisciplinaire **HAL**, est destinée au dépôt et à la diffusion de documents scientifiques de niveau recherche, publiés ou non, émanant des établissements d'enseignement et de recherche français ou étrangers, des laboratoires publics ou privés.

Bioinspired polydopamine nanoparticles: Synthesis, nanomechanical properties, and efficient PEGylation strategy

Islam Zmerli^a, Jean-Philippe Michel^a, Ali Makky^{a*}

^a Université Paris-Saclay, CNRS, Institut Galien Paris Sud, 92296, Châtenay-Malabry, France

* Corresponding author: ali.makky@universite-paris-saclay.fr

Abstract

Polydopamine (PDA) is a bioinspired fascinating polymer which is considered nowadays as a material of choice for designing drug delivery nanosystems. Indeed, PDA exhibits multiple interesting features including simple preparation protocols, biocompatibility, simple functionalization procedures, free radicals scavenging and photothermal / photoacoustic properties. However, because of its heterogeneous structure, clear procedures about PDA nanoparticles synthesis and PEGylation with well-defined and reproducible physicochemical properties such as size, shape and nanomechanics are still needed. In this work, we established tightly controlled experimental conditions to synthesize PDA nanoparticles with well-defined size and yield. This allowed us to identify the factors that affect the most these two parameters and to construct surface response plots with accurate predictive values of size and yield. The nanomechanical properties of PDA NPs exhibiting different sizes have been studied with AFM nanoindentation experiments. Our results demonstrated for the first time that the elasticity of PDA NPs was decreasing with their size. This could be explained by the higher geometric packing order of the stacked oligomeric fractions inside the core of the biggest PDA NPs. Next, in order to determine the best PEGylation experimental conditions of PDA NPs using thiol-

terminated PEG that allow grafting the highest polymer density with proteins repelling properties, we have first optimized the PEGylation strategy on PDA films. By using a combination of QCM-D and AFM experiments, we could demonstrate that efficient PEGylation of PDA films could be done even at low PEG concentration but in the presence of NaCl which exerts a salting out effect on PEG chains improving thus the grafting density. Finally, we transposed these experimental conditions to PDA NPs and we could synthesize PEGylated PDA NPs exhibiting high stability in physiological conditions as revealed by FTIR and DLS experiments respectively.

Introduction

Over the past decade, the conception of new nanomedicines for cancer therapy has been considered as one of the most rapidly evolving areas. Owing to the advances in nanotechnologies and insights into the pathology of cancer at the cellular and molecular levels, a large number of nanoscale carrier platforms have been developed such as liposomes, dendrimers, polymer nanoparticles and inorganic nanoparticles. However, compared to the number of papers dealing with the efficiency of these nanomedicines for treating several diseases, only few drug delivery systems for intravenous administration have been clinically approved¹⁻². This is mainly due to the complexity of the developed systems that present several issues regarding their synthesis at large scale, functionalization, heterogeneous composition / formulation, metabolism and long-term safety³. Many efforts have been thus devoted to design simple and multifunctional nanosystems based on one component strategy⁴⁻⁷.

In 2007, Messersmith et al.⁸ introduced a simple and pioneering method for surface functionalization which is bioinspired from the mussel adhesion process⁹⁻¹⁰. They demonstrated that dopamine can self-polymerize in aqueous medium and in mild alkaline conditions to form

polydopamine (PDA) polymer which can adhere onto various surfaces⁸ whether hydrophobic or hydrophilic. Later on, Ju et al.¹¹ have reported on the possible synthesis of polydopamine nanoparticles (NPs) that mimic melanin¹¹. Added to their functional properties¹²⁻¹³ such as free radical scavenging activity¹¹, photothermal conversion⁵ and photoacoustic imaging efficiencies⁵, PDA NPs present several advantages compared to other polymeric nanoparticles. Indeed, PDA NPs are easy to synthesize and are made from biodegradable and biocompatible polymers¹². Furthermore, the NPs diameter can be easily controlled by tailoring the experimental polymerization conditions such as the pH¹⁴, water/alcohol ratio, dopamine concentration and polymerization temperature¹⁵⁻¹⁶. Because of their ease of use and their fascinating properties, PDA NPs have attracted considerable interest for various biomedical applications¹³. In addition, PDA polymer exhibits a unique property which consists in its chemical versatility¹⁷. Indeed, the surface of polydopamine NPs can be easily modified for drugs and/or hydrophilic polymer grafting (i.e. PEGylation¹⁸) via covalent bonding with amines and thiols, hydrogen bonding, π - π stacking, metal coordination, and electrostatic interactions⁹. Actually, the PEGylation of nanoparticles¹⁹ is a commonly used approach for increasing their circulation time in the bloodstream and/or improving the efficiency of drug delivery to target cells and tissues¹⁸. It consists in coating the surface of nanoparticles with high surface density of polyethylene glycol (PEG) polymers that adopt a brush conformation. In the case of PDA NPs, some works^{11, 15} have been done in this direction by using high concentrations of thiol functionalized PEG (SH-PEG), however none of them provided a clear justification about their PEGylation strategy and the choice of the experimental conditions. The PEGylation of PDA can be done via “Grafting-To” strategy²⁰, which consists in grafting the polymer chain to the desired substrate. This can be done on PDA surface using either thiol (SH-PEG) or amine terminated PEG (NH₂-PEG) (Figure S1). Whereas SH-PEG can react *via* Michael addition with the catechol or with the corresponding

unsaturated indole rings, NH₂-PEG can be coupled to PDA using the same route but also *via* condensation reaction between the amine terminus group and the quinone to form Schiff base ⁸.¹². One of the big challenges to achieve a brush conformation of hydrophilic polymers is the excluded volume interactions, where the first grafted polymers at low density limit the access to the surface for other polymer chains thus leading to inefficient surface PEGylation ^{8, 21-22}. To overcome such problem, Pop-Georgievski et al. ²⁰⁻²¹ have achieved a dense grafted PEG polymer on planar PDA layer by using PEG melts which involves the heating of an ultrathin layer of PEG so the chains become mobile and exhibit ideal chain dimensions ²⁰⁻²¹. Despite its success, the melt approach requires a high working temperature which can be problematic for fragile encapsulated drugs and cannot be applied on nanoparticles. Besides, Ju et al.¹¹ have used high aqueous PEG-SH concentrations (up to 100 mg/ml for 1 mg/ml of PDA NPs) in order to reach the polymer cloud point ²³⁻²⁴ which may allow high grafting density of PEG on PDA NPs. However, this latter strategy requires a very high concentration of PEG polymer which is unfavorable for any industrial development.

In this work, we have first established tightly controlled experimental conditions to synthesize PDA nanoparticles with well-defined physicochemical properties. Next, we have identified the factors that affect the most the size and the yield of PDA NPs. Then the morphology and the nanomechanical properties of PDA NPs with different size have been studied using AFM. In fact, studying the nanomechanical properties of the NPs as drug delivery systems has gained a massive interest over the past years ²⁵⁻²⁸. Many relevant studies have reported about the impact of NPs elasticity on their cellular uptake, tissue penetration and biodistribution ^{27, 29-30}. Regarding PDA NPs, to the best of our knowledge, no previous studies have been reported neither about the elasticity of PDA NPs nor about the impact of their size on their mechanical properties. Finally,

we present a versatile PEGylation method of PDA film and NPs using heterobifunctional SH-PEG-COOH polymer by changing the ionic strength of PEG solution at room temperature. By using different complementary physical techniques including QCM-D and AFM, we have monitored the PEGylation kinetics of PDA film and we have demonstrated the efficiency of this strategy to graft PEG polymers at high density with nonfouling properties.

Material and methods

Chemicals

Dopamine hydrochloride (DA), Tris (tris(hydroxymethyl)aminomethane), (3-aminopropyl)triethoxysilane (APTES), N,N-diisopropylethylamine (DIPEA), glutaraldehyde (25% in water), Sodium dodecyl sulfate (SDS) and Poly (ethylene glycol) 2-mercaptoethyl ether acetic acid (SH-PEG_n-COOH, M_w = 2000, 3500 and 5000 Da) were purchased from Sigma Aldrich (St. Louis, Mo., USA). Sodium chloride (NaCl) was purchased from Carl-Roth Chemical (Karlsruhe, Germany), Ammonium hydroxide (25% NH₃) from Merck (Darmstadt, Germany) and ethanol from VWR Chemicals (Rafnor, Pa., UAS). Fetal bovine serum (FBS) was provided from Gibco (Invitrogen, Carlsbad, California, USA) and diluted to 10% (% vol) in Tris buffer (10 mM, pH 7.4). Ultrapure water was produced by a Millipore MilliQ Direct 8 water purification system with a resistivity of 18.2 MΩ.cm at 25 °C.

PDA NPs formulation

PDA NPs were synthesized following a previously established protocol^{5, 16}. Ultrapure water was mixed with ethanol (70/30 % v/v) and an aqueous solution of ammonia (25% NH₃). Dopamine hydrochloride was pre-dissolved in water and added to the abovementioned mixture under mild stirring. The reaction was allowed to proceed for 24 hours. Then, the preparations were purified

by centrifugal filtration in 30 kDa MWCO Amicon filters and subsequently washed with water for three times. Centrifugations were carried out at ~2000 g, 4°C for 20 min using SL-200 RFID rotor (NuAir Awel, UK). The volumes retained were redispersed in either ultrapure water or Tris buffer and then stored at 4°C.

To study the impact of experimental parameters on the size and yield of PDA NPs, we tested different dopamine concentrations (2, 2.5, 3.2, 4 and 5 mg/ml), molar ratios of ammonia/dopamine (10, 20, 25, 30, 38 and 50), and temperatures (25, 30, 40, and 50 °C). All PDA nanoparticles formulations were reproduced three times.

The yield in PDA NPs was calculated as follows after the freeze drying of a precise volume of the NPs suspensions (equation 1). NPs concentration was determined based on the lyophilizate mass.

$$Yield (\%) = \frac{m_{PDA}}{m_{Dopamine}} \times 100 \quad (1)$$

Dynamic Light scattering (DLS) and Zeta potential measurements

The hydrodynamic diameter (D_h) and surface charge were determined on aqueous NPs suspensions using a Zetasizer (Nano-ZS 90, Malvern Instruments, UK) with a detection angle of 90 °. The ζ -potential measurements were conducted in presence of low ionic strength (5 mM NaCl). All measurements were carried out at 25 °C and repeated three times. The hydrodynamic radius of PEG was measured in Tris buffer (10 mM, NaCl 150 mM) using Zetasizer (Nano-ZS, Malvern Instruments, UK) with a detection angle of 173° following the same procedure described by Kaszuba et al ³¹.

UV-visible absorbance

UV-visible absorbance spectra were recorded on a Cary 300 Bio UV-vis spectrophotometer (Varian, USA). The absorption of a NPs suspension was compared to that of an aqueous dopamine solution. The absorbance was measured for the wavelengths comprised between 200 and 800 nm.

Fourier Transform InfraRed spectroscopy

The FTIR analysis was performed on a Spectrum two spectrometer (PerkinElmer, France) in the attenuated total reflection (ATR) mode. NPs lyophilizate was analyzed and compared to dopamine hydrochloride powder. The spectra were recorded in the wavenumber range between 500 and 4000 cm^{-1} .

Atomic Force Microscopy (AFM)

Morphology and size distribution of PDA NPs prepared at different [Ammonia]/[Dopamine] ratios were examined ($T^{\circ}=25^{\circ}\text{C}$, $[\text{DA}]=3.2 \text{ mg/ml}$) using a JPK Nanowizard Ultraspeed AFM (JPK instruments, Germany). NPs were first diluted in ultrapure water to a final concentration around 350 $\mu\text{g/ml}$. 100 μl were then deposited on cleaved mica substrates (muscovite mica, grade V1 from Tedpella) and the samples were left to dry at room temperature. The samples were then imaged in air conditions in Amplitude Modulation AFM (AM-AFM) using gold coated silicon ACTG cantilevers (nominal spring constant $\sim 37 \text{ nN/nm}$, tip radius $< 10 \text{ nm}$) from AppNano (USA). Imaging was performed at low force settings (85–90% of the free amplitude set around 20 nm). Topographic images were analyzed with the JPK Data Processing software and the size distributions were determined manually by using the line profile option to obtain the NP height and full width at half maximum (FWHM) to avoid any tip convolution effect.

Cryogenic Transmission Electronic Microscopy (Cryo-TEM)

NPs were diluted to around 1 mg/ml in Tris buffer (10 mM, pH 7.4) and 5 μ l were deposited on a perforated carbon-coated copper grid (TedPella, Inc.). After removal by absorption of the liquid in excess, the grid was immediately immersed in a liquid ethane bath cooled at -180 °C. The grid was then mounted on a cryo holder and examined using a JEOL 2200FS (JEOL USA, Inc., Peabody, MA, U.S.A.) with an acceleration voltage of 200 kV. Micrographs were taken with a Gatan Ultrascan 2K camera (Gatan, Evry, France) and were treated with Image J software.

Evaluation of nano-mechanical properties of PDA NPs

The nanomechanical properties of PDA NPs prepared at different Ammonia/Dopamine molar ratios were carried out in a homemade fluid cell containing 200 μ l of Tris buffer, at room temperature using a JPK Nanowizard Ultraspeed AFM (JPK instruments, Germany) in JPK Quantitative imaging™ (QI) mode. QI is a multiparametric mode that collects force-distance (FD) curves in each pixel of a high resolution image with information about height, sample stiffness and adhesion. At each scanned pixel, the cantilever approached the surface until the vertical deflection reached the setpoint value, inducing sample's deformation, before being retracted away.

As PDA NPs could not be physically adsorbed onto mica in buffer, they were thus covalently attached to the chemically modified mica substrates. To do so, freshly cleaved mica substrates were silanized using (3-aminopropyl)triethoxysilane (APTES) in the presence of N,N-diisopropylethylamine (DIPEA). The silanization was carried out in vapor phase by applying a protocol described elsewhere³². In brief, in a plastic desiccator purged with nitrogen, 1 cm² cleaved mica surfaces were placed in presence of 60 μ l APTES and 40 μ l DIPEA and set under vacuum for 90 min. Immediately after removal from the desiccator, silanized mica substrates

were fixed on a glass slide and further functionalized by depositing 200 μl of glutaraldehyde in PBS buffer (1:1 v/v). After incubation for 2 hours, the substrates were rinsed with Milli-Q water. Afterwards, 100 μl of PDA NPs diluted to 0.5 mg/ml in Tris buffer (10 mM, pH 8.5) were deposited on the substrate and incubated for 1 hour. This method of functionalization allowed PDA NPs grafting to the surface *via* nucleophilic addition of the amine groups exposed on NPs surface onto the aldehyde function of the chemically modified mica substrates. Surfaces were then gently rinsed with ultrapure water, before adding Tris buffer (10 mM, pH 7.4) for AFM imaging.

The attached PDA NPs were thus imaged in QI mode at a resolution of $5\ \mu\text{m} \times 5\ \mu\text{m}$, 256×256 pixels using gold coated silicon ACTG cantilevers from AppNano (USA), with a nominal spring constant of $\sim 37\ \text{nN/nm}$ and a nominal tip radius of $\sim 10\ \text{nm}$. The force setpoint was fixed to 35 nN at an indentation speed of $50\ \mu\text{m/s}$. The spring constant of the cantilever was measured in Tris buffer at room temperature and determined before every experiment using the equipartition theorem (thermal noise)³³⁻³⁴ implemented in the JPK software Calibration Manager.

The Young's modulus associated with each pixel was determined with the JPK Data Processing software using the Hertz model. To do so, the approaching part of the force-indentation curves was fitted using the force-indentation relationship described in the Hertz model for the spherical indenter, as described by the following equation (2)

$$F = \frac{4}{3} \cdot \frac{E}{1-\nu^2} \cdot \sqrt{r} \cdot \delta^{\frac{3}{2}} \quad (2)$$

where ν is the Poisson's ratio set at 0.5 (a typical value retained for incompressible isotropic materials), δ the sample deformation induced by the indentation, r the tip radius estimated at 10

nm, F the force applied during sample indentation and E the elastic modulus also called apparent Young's modulus. This allowed the generation of the corresponding elasticity map.

As this model is valid for small indentations going up to 20 % of the material's height, we have chosen 35 nN as force setpoint in order to maintain sample deformation below 10 nm. At such small deformations, the result is not biased by the underlying substrate's rigidity and the contact area between the tip and the indented material does not exceed the tip radius.

PEG grafting in planar geometry using QCM-D

Quartz crystal microbalance with dissipation monitoring (QCM-D) is a highly sensitive instrument that allows real-time monitoring of the mass of deposited materials on an oscillating surface. This technique is based on the piezoelectric properties of a quartz sensor which oscillates, under the excitation by a sinusoidal current, in shear deformation mode with a fundamental resonant frequency of 5 MHz. During QCM-D experiments, resonance frequency is recorded with multiple overtones. Frequency changes (Δf) refer to mass adsorption or desorption on or from the surface. Simultaneously, the energy dissipation of this oscillatory system is obtained by switching off regularly the electric excitation. Dissipation shifts (ΔD) are related to the viscoelastic properties of the adsorbed material. In the case of hydrated layers with viscoelastic behavior, energy is dissipated with a time decay resulting in a high dissipation shift. Kelvin-Voigt model is commonly used to describe dissipative systems and interpret the obtained Δf and ΔD signals³⁵. In this model, the oscillatory system is described as a spring (corresponding to the elastic part) mounted in parallel to a dashpot (referring to the viscous part), with a complex shear modulus G^* defined by the following equation (3)

$$G^* = G' + i G'' = \mu_f + i 2\pi f \eta_f \quad (3)$$

where G' and G'' is the energy storage and energy dissipation moduli respectively, μ_f is the elastic shear modulus, f is the resonance frequency and η_f is the viscosity of the hydrated layer.

QCM-D was used for real-time analysis of PDA film formation, its subsequent functionalization with PEG chains and the ability of these coatings to inhibit proteins adsorption. QCM-D experiments were performed at 25 °C using a QCM-D E4 (Q-sense, Gothenburg, Sweden) and SiO₂-coated quartz crystals as sensors. Resonance frequency and dissipation changes were recorded for five overtones ($n = 3, 5, 7, 9$ and 11). Prior to use, SiO₂-coated quartz crystals were sonicated in 10 % SDS solution for 5 minutes and rinsed excessively with ultrapure water before being dried under N₂. The sensors were then treated with UV/Ozone for 40 min. Prior to use, QCM-D channels were cleaned using 2% Hellmanex solution and thoroughly rinsed with ultrapure water. Before the injection of the solutions, stable baselines were ensured to be reached in the buffer solutions. At the end of each experiment, a thorough rinsing step was performed using the corresponding buffer to eliminate loosely attached materials.

First, PDA film was formed on QCM-D sensor by injecting a 2 mg/ml dopamine solution in 10 mM Tris buffer at pH 8.5 using a peristaltic pump with a flow rate of 250 μ l/min. The dopamine solution was prepared *in situ* and set under stirring with access to oxygen. Rinsing was performed at a fixed frequency shift in order to obtain the same PDA layer thickness for all experiments ($\Delta f_5 \sim -100$ Hz, reached after ~ 2 hours of solution injection).

Next, a 1 mg/ml PEG solution in Tris buffer (10 mM, pH 8.5) was injected onto the pre-formed PDA film at a flow rate of 250 μ l/min. Δf and ΔD were recorded for ~ 17 hours, which was sufficient to reach saturation. Three molecular weights were tested for SH-PEG_n-COOH, $n = 2000$ Da, 3500 Da and 5000 Da, to compare their grafting efficiency on PDA film. The impact of salts concentration on PEG grafting on PDA surface was studied by injecting PEG solution in 10

mM Tris buffer supplemented or not with 150 mM NaCl. Experiments were repeated three times for each condition. The morphology and thickness of PDA and PEGylated PDA films were then studied by AFM imaging and nanoscratching experiments respectively.

Proteins adsorption was then evaluated for bare PDA film and PEG functionalized films by injecting fetal bovine serum (FBS) diluted to 10 % (% vol) in Tris buffer (10 mM, pH 7.4). Based on the results obtained from these experiments, PEG chain length and grafting conditions were selected for PDA NPs PEGylation.

PEG chains conformation was theoretically estimated by calculating their overlap parameter defined by the ratio $D/2R_g$, where D is the distance between two neighboring chains and R_g their gyration radius^{20, 36}. It is assumed that (i) for $D/2R_g > 1$, PEG macromolecules adopt a mushroom conformation on the functionalized surface, (ii) for $D/2R_g = 1$, they are in a mushroom-to-brush structural state, while (iii) for $D/2R_g$ values < 0.5 , the grafting density is very high forcing the polymer chains to adopt a brush conformation.

In a good solvent, $R_g = 1.78 R_h^{20}$ where R_h is the hydrodynamic radius of the PEG coil determined by DLS. D can be calculated as follows:

$$D = \sqrt{\frac{4}{\pi \cdot \sigma}} \quad (4)$$

where σ is the grafted density of PEG³⁷ given as:

$$\sigma = \frac{1}{A_{PEG}} = \frac{N_{PEG}}{S} \quad (5)$$

where A_{PEG} is occupied area per PEG chain, N_{PEG} is the number of PEG molecules grafted on the surface (S)³⁷. N_{PEG} was calculated from the mass of the PEG layer deduced from the fitting of the QCM-D data with Voigt-Voinova model³⁵ using Q-Tools software (3.0.15).

The thickness value obtained by AFM nanoscratching experiments for the PEG layer was injected in the Voigt model equations to allow the calculation of the layer's density, viscosity and shear modulus. The density and viscosity of the aqueous phase were set at 1000 kg.m^{-3} and $0.001 \text{ kg.m}^{-1}.\text{s}^{-1}$, respectively.

The thicknesses PDA and PDA-PEG films were determined simultaneously in the presence of buffer and after drying with nitrogen stream, in order to calculate the swelling percentage ($\%_{\text{H}_2\text{O}}$) following the equation 6:

$$\%_{\text{H}_2\text{O}} = \left(\frac{H_{\text{hydrated layer}} - H_{\text{dry layer}}}{H_{\text{dry layer}}} \right) \times 100 \quad (6)$$

PEGylation of PDA NPs

After optimization of NPs formulation, PDA NPs of an average diameter of ~140 nm were used for further functionalization with SH-PEG₂₀₀₀-COOH. After purification, bare PDA NPs were dispersed in Tris buffer (10 mM, 150 mM NaCl, pH 8.5). PEG₂₀₀₀ was dissolved in the same buffer and added to the NPs suspension. The final concentrations were 1 mg/ml and 10 mg/ml for PDA NPs and PEG solution, respectively. The mixture was allowed to react at room temperature under mild stirring. After 24 hours, the NPs were purified by centrifugal filtration (MWCO 30000 Da). NPs diameter and zeta potential were measured using the same protocol described for PDA NPs. NPs PEGylation was further assessed by FTIR spectrometry and DLS.

Statistical analysis

In order to assess the significance of sizes and yields observed between the different groups of PDA NPs, we have conducted a one-way analysis of variance (ANOVA) using the data analysis toolkit in Microsoft® Excel. *p*-value less than 0.01 was considered statistically significant.

Results and discussion

PDA nanoparticles synthesis: impact of polymerization conditions on their size and yield

Polydopamine also referred as dopamine-melanine is an heterogenous biosinspired polymer which can be easily synthesized from dopamine monomer in alkaline conditions ⁸. Despite the fact that its exact structure is not yet fully elucidated ³⁸⁻³⁹ due to the complexity of the polymerization pathways and its insolubility in aqueous and organic solvents, there is a general agreement that PDA formation involves the oxidation of protonated dopamine monomers in alkaline aqueous conditions to give dopamine-quinone molecules which can further cyclize to form dihydroxyindole (DHI) molecules as key precursors of PDA ⁴⁰⁻⁴². Different experimental conditions for PDA NPs synthesis have been described so far, and most of them consisted in the oxidation of dopamine in aqueous solution in the presence of a strong base such as NaOH or NH₄OH ^{11, 14-15}. However, these protocols usually lead to the formation of large aggregates coexisting with the desired NPs which induced a loss in the final NPs yield and required further purification steps to remove the large aggregates ^{11, 14-15}. Recently, by calculating the Hansen solubility parameters of the solvents, Jiang et al.¹⁶ have demonstrated the importance of water/alcohol mixture for PDA NPs synthesis. They have found that a volume ratio of alcohol/water about 30% was necessary in order to obtain spherical PDA NPs without the formation of large aggregates ¹⁶. Thus, based on this study we have chosen water/ethanol at a volume ratio of 30% as solvent for the synthesis of PDA NPs and we have assessed the effects of dopamine concentration, the reaction temperature and the base/dopamine molar ratio on the size and yields of NPs. To do so, we studied first the impact of dopamine concentration on the size and yield of NPs at a constant [Ammonia]/[Dopamine] ratio (R=25) and a temperature (T = 25°C) by measuring the size and the yield of the purified NPs after 24 hours of incubation. Results are presented in Figures 1A and 1B.

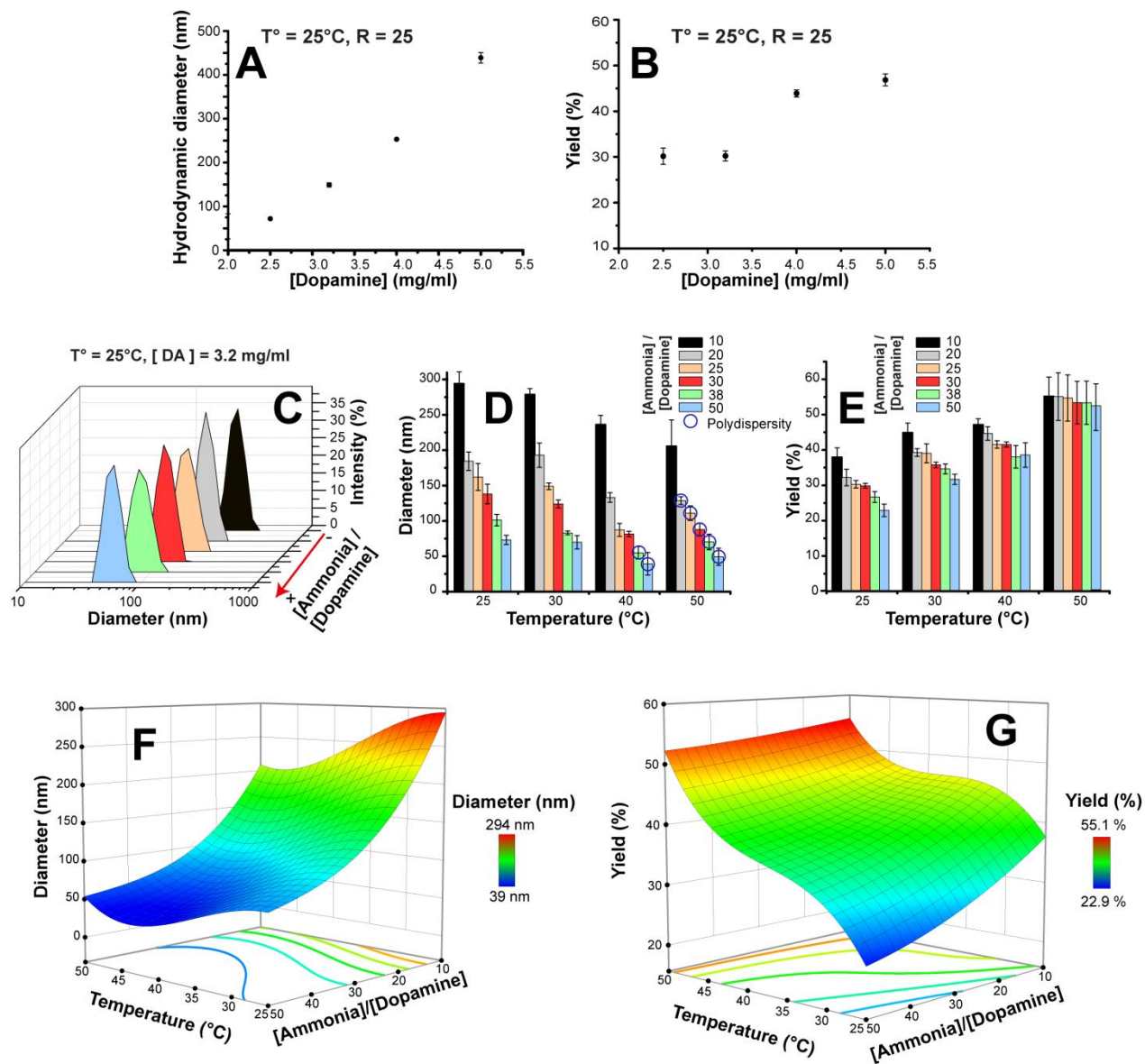


Figure 1: A. Hydrodynamic diameter and B. Yield of PDA NPs prepared at 25°C with [Ammonia]/[Dopamine] ratio of 25, as a function of dopamine concentration. C. An example of DLS data of PDA nanoparticles as a function of [Ammonia]/[Dopamine] ratio. PDA NPs were prepared at a temperature of 25°C and a dopamine concentration of 3.2 mg/ml. (D,E) Histograms representing the hydrodynamic diameter and yield variations as a function of preparation temperature and [Ammonia]/[Dopamine] ratio at a dopamine concentration of 3.2 mg/ml. (F,G) Surface

response plots showing the effect of the temperature and the [Ammonia]/[Dopamine] ratio on the NPs hydrodynamic diameter and yield.

After the addition of dopamine at different concentrations ranging from 2 to 5 mg/ml to the reaction mixture, the colorless solutions turned rapidly to pale brown then gradually to dark brown and finally black indicating the formation of PDA features. After 24 hours of incubation, the PDA NPs were purified with centrifugal filtration in order to eliminate the unconverted dopamine derivatives and were characterized in terms of their hydrodynamic diameter by DLS and their yield after freeze drying. While a dopamine concentration of 2 mg/ml did not lead to the formation of monodisperse PDA NPs, those ranging from 2.5 to 5 mg/ml gave rise to monodisperse NPs with a hydrodynamic diameter increasing with the concentration of DA (Figure 1A). However, the yield did not follow the same tendency (Figure 1B) but reached higher values (~45%) with higher concentrations of dopamine. The reaction time was also determined, and as shown in the Table S1 and Figure S2, neither the yield nor the NPs size changed after 30 H of reaction which implies that the polymerization reaction of DA did not progress further after 24 H. Based on these results and as the concentration of DA at 3.2 mg/ml gave monodisperse NPs distribution with a mean hydrodynamic diameter ≤ 200 nm which is considered as optimal NPs diameter for intravenous administration in *in vivo* applications, this concentration and the reaction time of 24 H were kept constant in this study. Figure 1C shows the hydrodynamic diameter measured by DLS of the purified PDA NPs that were prepared with increasing [Ammonia]/[Dopamine] ratios. Indeed, NPs hydrodynamic diameter was strongly dependent on [Ammonia]/[Dopamine] ratio, with a NPs size decreasing from ~300 nm to ~60 nm for ratios comprised between 10 and 50 respectively, at 25°C. The effect of base concentration is consistent with previous reports in the literature^{11, 14}. Actually, under alkaline conditions and in presence of

oxygen, dopamine hydrochloride is deprotonated, oxidized and self-polymerized leading to the production of polydopamine. The redox process is associated with protons production. Basic pH allows thus the consumption of the produced protons and the shift of the redox reaction equilibrium towards the production of polydopamine. Hence, higher pH values will enhance the nucleation of PDA nanoparticles and lead to the formation of smaller NPs. Moreover, polydopamine is more soluble in high basic pH, which may promote the formation of smaller NPs as the amount of ammonia increases⁴³. As the proton release from dopamine hydrochloride decreases the solution pH, this will result in decreasing the dopamine polymerization process and thus affording unchanged size of PDA NPs. Similar to the effect of the [Ammonia]/[Dopamine] ratio, increasing the reaction temperature from 25°C to 50°C resulted in the decrease of NPs size for the respective [Ammonia]/[Dopamine] ratios but also with a loss in size monodispersity for temperatures exceeding 40 °C as shown in Figure 1D and table S2. The monodispersity loss of PDA NPs at high temperature could be related to the evaporation of ethanol and/or of the ammonia with time, which may reduce the PDA solubility and thus a loss in their size control. Conversely, as depicted in Figure 1E, the yield of PDA NPs increased with the reaction temperature and was inversely proportional to [Ammonia]/[Dopamine] ratio. An increase in the reaction temperature thus provides more energy to the system and probably accelerates the kinetics of polymerization, generating NPs smaller in size but in greater number than at low temperature. Different results have been reported in the literature regarding the yield of PDA NPs as a function of [Ammonia]/[Dopamine] ratio. While Jiang et al.¹⁶ observed unchanged yields when varying the pH reaction, Ju et al.¹¹ reported an increase of the yield with the pH and temperature. Such discrepancy may be related to the different employed purification methods but also to the formation of non polymerized amorphous agglomerates at high pH values that can pass through the filters membranes. In order to assess the difference significance between sizes

and yields of the different groups of PDA NPs, we have conducted a one-way analysis of variance (ANOVA). By analyzing the impact of temperature and [Ammonia]/[Dopamine] ratio on the sizes and yields of PDA NPs, we found that the size differences between the PDA NPs groups as well as their yields were significant except for the yields obtained at 50°C. The results are summarized in the table S3 and S4.

As the [Ammonia]/[Dopamine] ratio and the reaction temperature significantly affected the size and yield of PDA NPs, their impact was further assessed by generating surface response plots (Figure 1F, 1G) from the whole set of data, using a central composite design with two numerical factors ([Ammonia]/[Dopamine] ratio and temperature). This allows the prediction of the size or the yield from these two parameters. Indeed, by using the size-factor and yield-factor relation equations generated from the central composite design analysis (Equations in SI), it is possible to determine the range of values of the two experimental parameters allowing the synthesis of PDA NPs with the desired size and yield. In order to confirm the efficiency of the generated size-factor and yield-factor relationships, five different synthesis experiments were conducted and the results were compared to the predicted ones. The experimental results were fully consistent with predicted size and yield values using central composite design analysis. Thus, our data set provides a simple and accurate method to produce PDA NPs with a fine control of their size and yield.

T (°C)	[Ammonia] / [DA]	Predicted D _h (nm)	Experimental D _h (nm)	Predicted yield (%)	Experimental yield (%)
25	14.0	250	264±6	35.7	36.1±0.6
25	19.0	200	211±1	33.3	33.8±1.1
32	12.0	250	258±8	44.9	45.5±0.7
32	17.0	200	193±7	42.8	43.0±0.5
32	33.5	100	115±2	37.0	38.2±0.8

Table 1: Comparison of experimental values of NPs size and yield obtained for different [Ammonia]/[Dopamine] ratios with those generated from response surface models.

Morphological characterization of PDA nanoparticles

After the optimization of the formulation conditions of PDA nanoparticles, their size and their morphology were assessed using transmission electron microscopy (Cryo-TEM) and atomic force microscopy (AFM). Cryo-TEM experiments were performed on PDA NPs obtained at 25°C with a [Ammonia]/[Dopamine] ratio of 25. The cryo-TEM image presented in Figure S3 shows spherical NPs with monodisperse size around 150 nm and a rough surface. Although the DLS data of the different batches of PDA NPs were all monodisperse, several studies however pointed out the limitations of the scattering techniques in resolving the NPs size distribution⁴⁴⁻⁴⁶ accurately. Indeed the DLS signal intensity is related to the sixth power of the particle diameter, thus the presence of some large particles in the same sample will scatter higher amount of light, thus inducing an overestimation of the NPs size measured by DLS^{45, 47-48}. In order to circumvent this limitation, PDA NPs were prepared at a temperature of 25°C and with different [Ammonia]/[Dopamine] ratios and absorbed onto freshly cleaved mica for AFM imaging in air in amplitude-modulation AFM. As shown in Figure 2A-2F, AFM images revealed well dispersed particles with semi-spherical shapes.

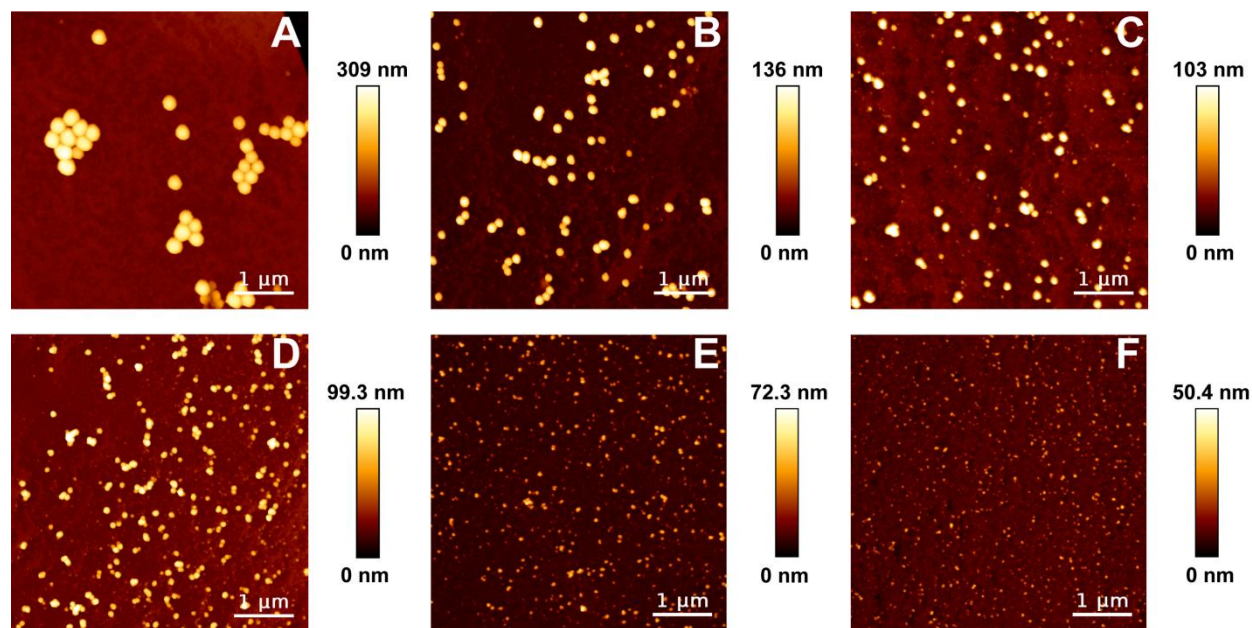


Figure 2. AM-AFM topographical images in air of adsorbed PDA NPs onto mica substrates. The NPs were at a temperature of 25°C but at different [Ammonia]/[Dopamine] ratios A(10), B(20), C(25), D (30), E (38), F(50).

Similar to DLS results the size of NPs was reduced as the [Ammonia]/[Dopamine] ratio increased. However, it should be noticed that the coexistence of few small polymeric features with very low height ($h < 20$ nm) was also observed in AFM height images. These latter became more frequent as the size of the PDA NPs decreased. This may be due to the presence of some PDA oligomeric stacks that were not fully grown into PDA NPs and could not be removed by the adopted purification methods. Next we performed a statistical analysis of the height and width of the different batches. In order to reduce the convolution effect on the lateral size of nanoparticles imaged by AFM, the widths were all measured at the full width at half maximum (FWHM) of the peak height⁴⁵. The obtained results are summarized in Table 2 and Figure S4. All NPs heights and widths could be nicely fitted with one symmetric Gaussian peak (Figure S4). Compared to the DLS data, those obtained with AFM were lower. This discrepancy could be explained by the polydispersity index of the studied samples. As already mentioned, DLS overestimates the NPs size distribution by favoring the light diffusion of larger objects^{45, 47-48}. Furthermore, the drying

step necessary to adsorb NPs on mica surface, as well the interaction with mica surface after adsorption may generate noticeable changes in their shape and dimensions on AFM pictures. Taken together, both DLS and AFM data confirmed the fact that increasing the [Ammonia]/[Dopamine] ratio induced a decrease in the PDA NPs diameter and that they exhibited spherical shape with monodisperse distribution.

[Ammonia] / [Dopamine]	DLS			AFM	
	D _h (nm)	PDI	ζ (mV)	FWHM (nm)	Height (nm)
10	294±17	0.021±0.019	-35.9±1.1	253±18	205±11
20	184±13	0.030±0.023	-33.9±1.0	146±15	105±8
25	162±19	0.028±0.019	-36.2±1.3	121±12	89±10
30	138±14	0.052±0.022	-36.8±0.6	105±11	64±10
38	101±8	0.072±0.025	-36.1±1.4	70±8	42±9
50	73±7	0.145±0.049	-33.1±1.3	55±6	26±4

Table 2: Summary of the size and zeta potential values of PDA NPs prepared at a temperature of 25°C and at different [Ammonia]/[Dopamine] ratios as measured by DLS in ultrapure water and AFM in air.

Finally, the zeta potential of PDA NPs was measured at 25°C for different [Ammonia]/[Dopamine] ratios (Table 2). All PDA NPs exhibited negative zeta potential values that could be related to the deprotonation of the catechol groups exposed at their surfaces^{14, 49}. Independently of their size, the ζ values remain almost unchanged (around -36 mV) which indicates that PDA NPs expose the same functional groups at their surface.

Nanomechanical properties determination of PDA nanoparticles

Besides, the nanomechanical properties of PDA NPs exhibiting different sizes were examined performing AFM nanoindentation experiments^{26, 50}. Measuring the Young's modulus of NPs with different sizes is of great interest for biomedical applications²⁵⁻²⁷. Indeed, several studies have highlighted the influence of NPs nanomechanics on their structural and functional properties²⁵⁻²⁷ all the more so polymeric nanomaterials may behave differently from their bulk counterparts⁵¹⁻⁵². The AFM nanoindentation experiments consist in force spectroscopy measurements in

which the AFM tip approaches the sample and is pushed into it, until a predefined force is reached and then the tip is retracted thus generating force-distance curves (Figure 3B). These latter can be fitted with different contact mechanics models namely with Hertz⁵³, Johnson–Kendall–Roberts (JKR)⁵⁴ or Derjaguin–Muller–Toporov (DMT)⁵⁵ models. So far, Hertz model is the most used one because of its simplicity, however different experimental conditions such as indentation depth, tip geometry, cantilever stiffness should be precisely defined in order to avoid any wrong estimation of the calculated Young’s modulus^{50, 56}. Indeed, the Hertz model assumes a spherical shape for the AFM tip and a non-adhesive contact between the indenter and the sample⁵⁰. Thus, in order to determine the best experimental conditions for nanoindentation experiments, we first performed AFM imaging of covalently attached PDA NPs ($D_h = 131 \pm 2$ nm) with low force settings in buffer using quantitative imaging AFM mode (QITM)⁵⁷⁻⁵⁸ which collects force-distance (FD) curves in each pixel in a high resolution image with information about height and sample stiffness (Figure 3B). Afterwards, we analyzed force-distance curves at the center of several individual NPs. As shown in Figure 3B, by applying a force of 35 nN on PDA NPs induced a height deformation of ~10 nm which represents only 10% of the sample total height (~110 nm). This condition is essential to exclude the substrate effect on the mechanical measurements. In addition, this indentation depth is almost equal to tip radius of the used cantilever which was assumed to 10 nm as nominal value, hence the indenter geometry could be assumed as sphere and the Hertz model could be applied⁵⁰.

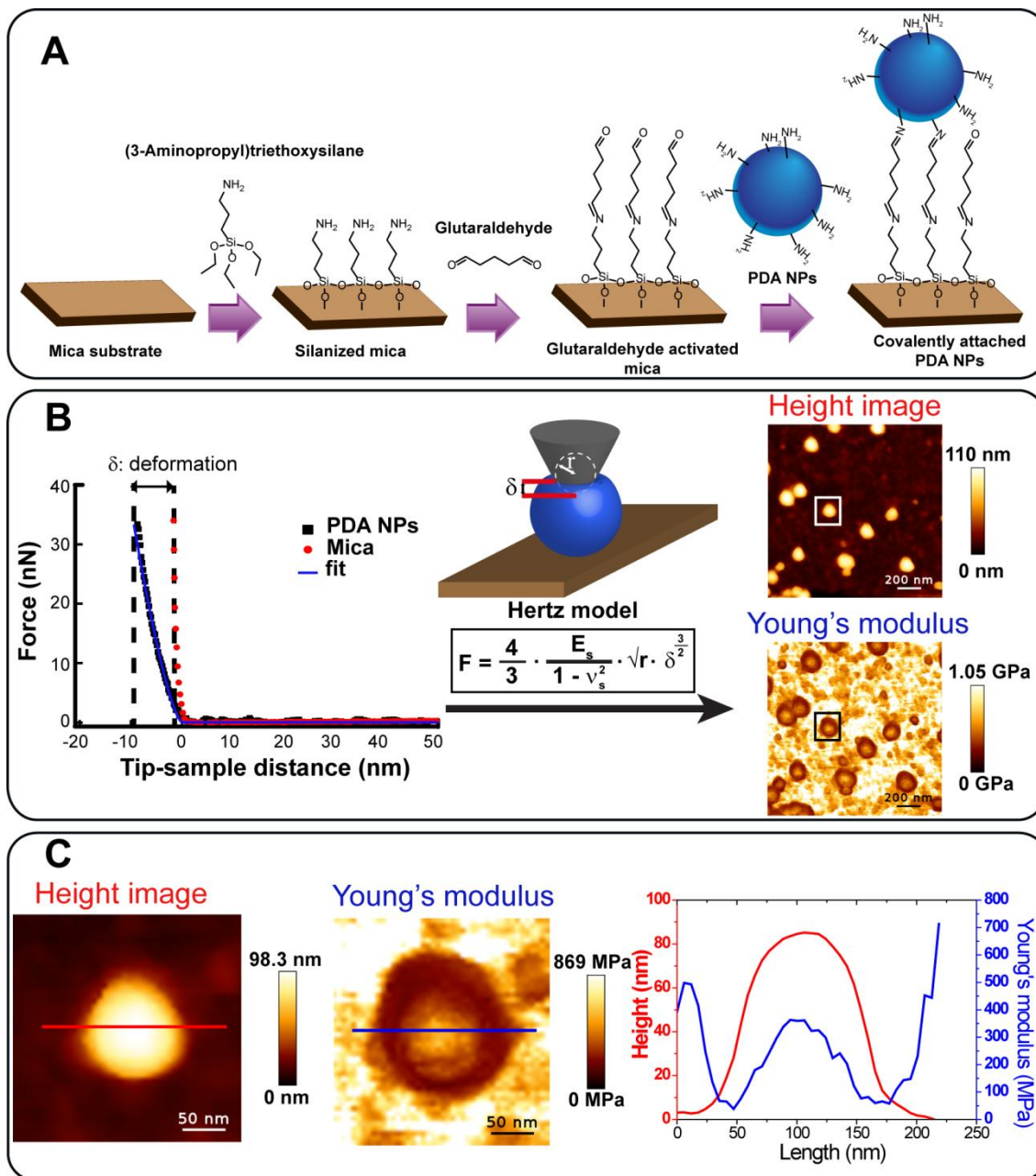


Figure 3. A. Scheme illustrating the functionalization strategy of mica substrates for the covalent attachment of PDA NPs (images not to scale). B. Typical experimental force distance curves obtained on mica (red) and on the top of PDA NPs (black) with the fit (blue) using the Hertz model. Representative topography image with the corresponding elasticity map obtained with QI mode at a force setpoint of 35 nN at an indentation speed of 50 $\mu\text{m/s}$. C. QI imaging of PDA NPs with the height image and elastic modulus maps and associated cross sections along the red and blue lines drawn on maps.

The elastic modulus maps of PDA NPs (Figure 3C) revealed higher Young's modulus values in their centers compared to their edges. Such observation could be related to geometrical artifacts during the contact between the tip and the nanoparticles edges. Indeed, the contact between the tip and the top of the NPs satisfies at utmost the condition of symmetric form of the indenter required by the Hertz model.

Full Force-Distance curves performed on individual NP are depicted in Figure S5. Compared to force curves recorded on mica at a speed of 50 $\mu\text{m/s}$, those obtained on PDA NPs exhibited a slight hysteresis between the approach and the retract curves (Figure S5). Such behavior could be related either to a plastic deformation of PDA NPs or to the cantilever inertia and/or to the viscous relaxation time of the sample due to the high speed of the force indentation measurements acquired in Quantitative imaging (QI) mode. Thus, in order to investigate the source of such hysteresis, we have performed a series of nanoindentation experiments at different loading rates (62.5, 31.25 and 15.625 $\mu\text{m/s}$). As depicted in the Figure S6, the hysteresis is reduced as the indentation speed decreases. In addition the determined Young modulus values were not changed significantly at the different loading rates as analyzed by the unpaired two sample Student's t-test. This demonstrates that the mechanical properties of PDA Nps are not dependent on the indentation speed (Figure S6). Furthermore, the imaged PDA Nps did not exhibit any significant difference in shape or height following two consecutive AFM images acquired in Quantitative imaging (QI) mode. This result rules out the hypothesis of plastic deformation (Figure S7).

Using QI mode, the height and Young modulus maps of different PDA NPs with decreasing size were determined (Figures 4A-4D for the height maps, Figures 4E-4H for the Young's modulus ones). Young's modulus values at the maximal height of each NPs type were measured and their

distributions were represented as histograms with their Gaussian fits (Figure 4I-4L). Interestingly, the Young's modulus of PDA NPs was decreasing with their size.

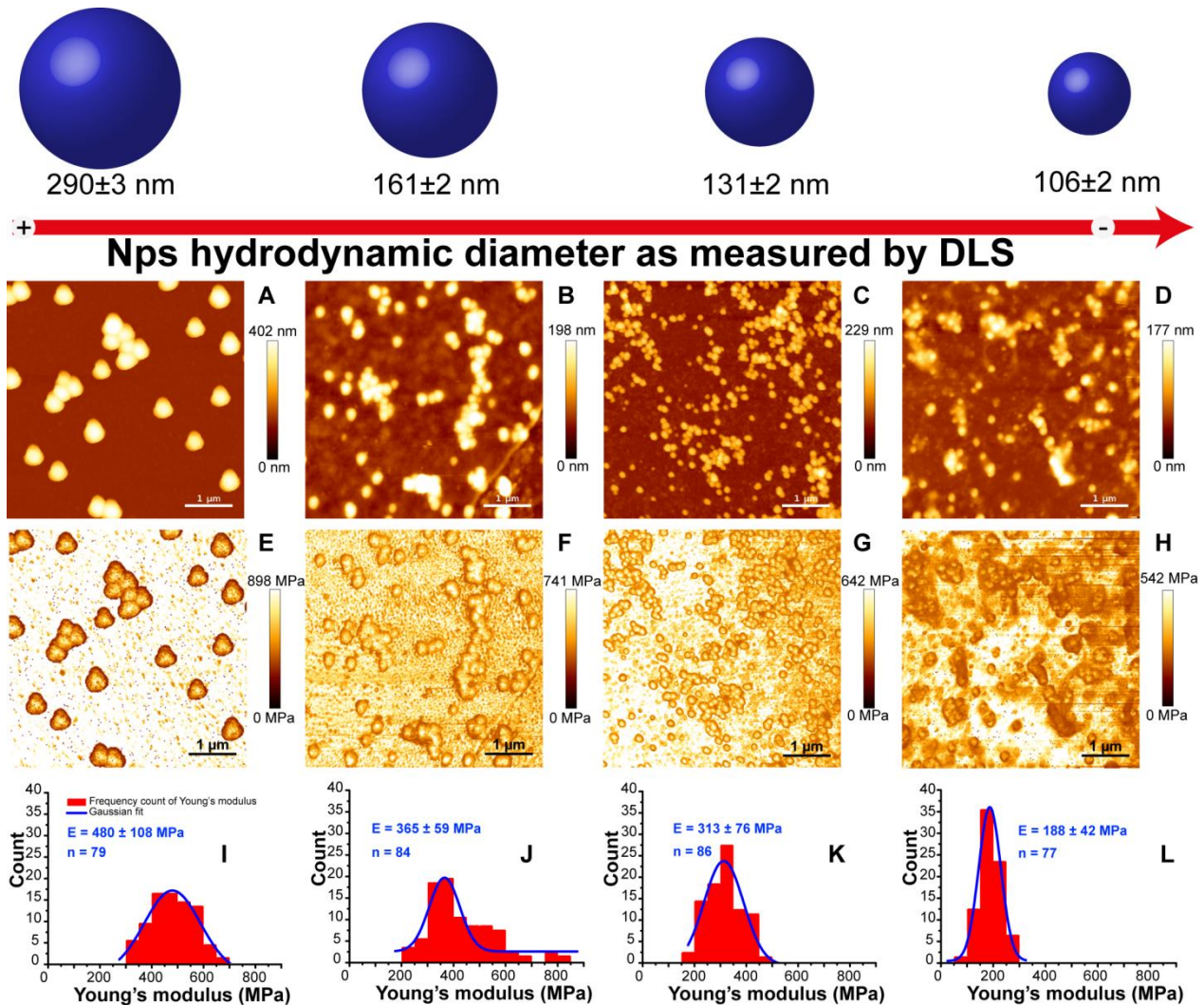


Figure 4. AFM height images in Tris buffer (10mM, NaCl 150 mM) of covalently attached PDA NPs with different sizes (A, B, C, D) on silanized mica substrates with their corresponding Young's modulus maps (E, F, G, H) obtained with JPK Quantitative imaging™ (QI) mode at a force setpoint of 35 nN at an indentation speed of 50 $\mu\text{m/s}$. (I, J, K, L) represent the histograms distribution of the Young's modulus of NPs with Gaussian fits.

In greater details, PDA NPs with a mean D_h of 290 ± 2 nm exhibited a Young's modulus (E) of 480 ± 108 MPa, followed by NPs having hydrodynamic diameters of 161 ± 2 nm and 131 ± 2 nm with Young's modulus values of 365 ± 59 MPa and 313 ± 76 MPa, respectively. The smallest

PDA NPs having a D_h of 106 ± 2 nm exhibited the lowest Young's modulus of 188 ± 42 MPa. Compared to other polymeric nanomaterials made of PMMA, PLGA or polystyrene, the Young's modulus values for PDA NPs are almost one order of magnitude lower. This strong difference in mechanical behavior could be mainly related to the nature of polymer but also to their self-assembly process. PDA exhibits a complex and heterogeneous structure which makes the elucidation of its polymerization mechanism still unresolved³⁸. Many authors have proposed that PDA is not a covalent polymer but rather a supramolecular aggregate of monomers, oligomers consisting of dihydroxyindole (DHI), dopamine quinone, dopamine and other eumelanin-like derivatives that are held together through weak interactions such as charge transfer, π -stacking, hydrogen bonding and π -cation^{39, 41}. However, others have suggested that PDA exhibit a polymeric structure of high molecular weight arising from aryl-aryl linkages between the oxidized and cyclized dopamine monomers³⁸. Conversely, Hong et al.⁴² suggested that PDA consists in mixtures made of covalently bound indole units, physical trimers made of two dopamine molecules and on dihydroxyindole which are held together by π -stacking and hydrogen bonding⁴². Besides, Waren et al.⁵⁹ have recently studied by the mean of pump-probe microscopy the role of the aggregation state of the oligomeric structures inside Melanin-like nanoparticles with different sizes (30 nm, 100 nm or 250 nm) generated by spontaneous dopamine oxidation on their absorption properties. By exploring the broad absorption bands of these NPs and their disassembled subunits including monomers, oligomers and stacked oligomers also known as protomolecules⁵⁹, they suggested that larger PDA NPs showed higher attenuation at longer wavelengths compared to smaller ones due to their higher geometric packing order⁵⁹. Similarly, this finding could explain also the dependence of Young's modulus values with NPs size, in particular for the bigger PDA NPs that exhibit higher elastic modulus values because of the

higher geometric packing order of the stacked oligomeric fractions inside the core. The higher is this packing order, the more rigid are the NPs.

PEGylation strategy of PDA nanoparticles

The next step was focused on the optimization of PDA PEGylation strategy in order to obtain high density of PEG chains grafted at the PDA surface. Since the PEG grafting efficiency as well as the PEG density on PDA NPs cannot be easily assessed with conventional techniques (i.e. DLS, AFM, Cryo-TEM), we investigated the PEGylation kinetics and efficacy of PDA planar adlayer using QCM-D in combination with AFM (Figure 5A). This combination allows the determination of the best PEGylation conditions leading to the highest PEG density on PDA surface. Thus, we have monitored *in situ* the formation of PDA film on SiO₂-coated quartz crystals upon the oxidation of dopamine in Tris (pH 8.5) which is a commonly used buffer for surfaces coating with PDA. Herein, Tris was chosen instead of ethanol/water/ammonia mixture, because the dopamine polymerization in this latter mixture does not allow the formation of PDA film on SiO₂-coated quartz crystals. Moreover, both polymerization procedures led to PDA assemblies exhibiting similar FTIR spectra^{8,11}, thus indicating that the chemical structure of both PDA preparations is comparable. Hence, the PDA film can be used as a chemical model of PDA Nps.

Figure 5B represents the change in Δf and ΔD following the injection of dopamine in Tris buffer (pH 8.5). Dopamine injection on SiO₂-coated quartz crystals led to a progressive decrease in Δf which reaches a $\Delta f_5 \sim -100$ Hz and an increase in the corresponding ΔD value of $\sim 10 \times 10^{-6}$ which remain constant after buffer rinsing. This indicates the formation of stable PDA film on the SiO₂-coated quartz crystal. Indeed, under alkaline conditions the dopamine monomer is spontaneously oxidized by dissolved oxygen which leads to highly reactive products formed at

the end of the oxidation cascade such as 5,6-dihydroxyindole and quinone derivatives (5,6-indole-semi-quinone and 5,6-indole-quinone) which further polymerize into oligomers or polymers. These latter self-assemble and form colloidal particles that form thin layer on the surface in contact with the solution and can further aggregate to precipitate in the solution. In order to avoid the formation of such large particles on the top of the quartz, the experiment was stopped after two hours of dopamine injection.

The PEGylation of PDA film was done using heterobifunctional PEG (SH-PEG_n-COOH) polymers with different molecular weights (2000, 3500 or 5000 Da) and bearing a thiol group at one extremity and a carboxylic group at the other one. Whereas the thiol group will serve as chemical anchor for the PEG chain on the catechol groups of PDA film *via* Michael addition reaction, the carboxylic group can be used for coupling other ligands on the PEG extremity. Figure 5C displays the adsorption kinetics of the different SH-PEG_n-COOH polymers on PDA film after the injection of PEG solution at a concentration of 1 mg/ml in Tris buffer in the absence of salts. Compared to the neat SiO₂-coated quartz crystal, the injection of thiolated PEG polymers on PDA adlayer induced an abrupt decrease in the 5th overtone frequency (Δf_5) with subsequent increase in the corresponding dissipation (ΔD_5) suggesting the specific adsorption/attachment of the SH-PEG onto PDA film. Moreover, these changes were dependent on the PEG molecular weights. Indeed, by increasing PEG molecular weight, the changes in Δf_5 and ΔD_5 were more important. Moreover, while the injection of SH-PEG₂₀₀₀-COOH revealed a rapid saturation after 5 hours of injection, SH-PEG₃₅₀₀-COOH and SH-PEG₅₀₀₀-COOH exhibited slower saturation kinetics and tend to reach a plateau only after 14 hours of injection. Interestingly, the time-dependent profiles (Figure 5C) as well as the final frequency shifts and

dissipation values, revealed that the three PEG polymers behave similarly and reached similar Δf and ΔD levels. These results demonstrate that the highest grafting molecular density of PEG could be obtained with the polymer having the lowest molecular weight (i.e. PEG₂₀₀₀). However, the frequency and dissipation shifts obtained in this study were lower than those obtained by other authors when forming PEG brushes on gold substrates²². Our PEGylation conditions led to lower grafting density of PEG polymer on PDA. This could be mainly related to the excluded volume effect. Several approaches have been suggested in the literature in order to suppress or at least reduce the excluded volume effect between PEG chains²²⁻²⁴. Indeed, one could produce high grafted polymer densities by reaching the polymer cloud point which could be done using either highly concentrated solutions of functionalized PEG polymers, mixture of functionalized PEG in the presence of additional inert homopolymer²³ or by using lower concentration of functionalized PEG but in the presence of high salt concentration²². Since the two first approaches use high concentration of polymer, this may complicate the purification procedure of PEGylated materials and could not be favorable for the industrial development. We thus decided to modify our PEGylation strategy by preparing the SH-PEG₂₀₀₀-COOH solution at 1 mg/ml but in the presence of 150 mM of NaCl which may induce a salting out effect on PEG chains²². Figure 5D represents changes in Δf_5 and ΔD_5 following the injection of SH-PEG₂₀₀₀-COOH solution in the absence or the presence of 150 mM of NaCl. The injection of PEG in the presence of NaCl induced higher frequency and dissipation shifts than those obtained in the absence of salts suggesting a higher absorption of PEG molecules onto PDA surface. Moreover, the presence of salts significantly modified the kinetics of adsorption. While the injection of SH-PEG₂₀₀₀-COOH in the absence of NaCl reached a fast saturation after almost two hours with a Δf_5 of ~ -17 Hz (histograms), the presence of NaCl delayed the saturation level and induced almost ~ 3 folds

higher decrease in Δf_5 (~ -50 Hz) which remain stable after rinsing with buffer. Hence, the presence of 150 mM NaCl favors higher amounts of PEG chains grafted onto PDA surface.

To gain further insights about the morphology and the thickness of PDA and PDA-PEG films, the formed adlayers on the SiO₂-coated quartz crystals were characterized simultaneously by AFM imaging and nanoscratching experiments respectively. As shown in Figure S8, the PDA film exhibits a continuous rough surface (RMS $R_q = 2.4$ nm) with presence of some small colloidal particles. By performing nanoscratching experiments on multiple substrates we could determine the average thickness ~ 13.9 nm of the PDA film in buffer condition. Such PDA thickness is in accordance with those obtained by other authors on Si/SiO₂ substrates measured by ellipsometry²¹ for the same incubation duration. The normalized changes in frequency (Δf) and dissipation (ΔD) for the three overtones ($n = 5, 7, 9$) following the formation of PDA film, were plotted (Figure S9A). No overlap of the three overtones could be observed which indicates that the formed film behave as viscous layer adsorbed on the QCM-D quartz crystal. Thus, the Sauerbrey equation is invalid in this case for the calculation of adsorbed mass of PDA, as this assumes that the normalized changes in frequency (Δf) should be independent of overtones. Thus we fitted the experimental results in Figure S9A using the Kelvin-Voigt model as a more realistic model to describe the formed PDA film. The best fit results yield the changes in adsorbed mass (Δm_{PDA}), the shear modulus (μ_{PDA}), and shear viscosity (η_{PDA}). The fitting results were in excellent agreement with the measured data for all three overtones demonstrating the validity of the model, yielding $\Delta m \sim 2750$ ng/cm² and a density ~ 2000 Kg/m³ for the PDA layer (Table 3).

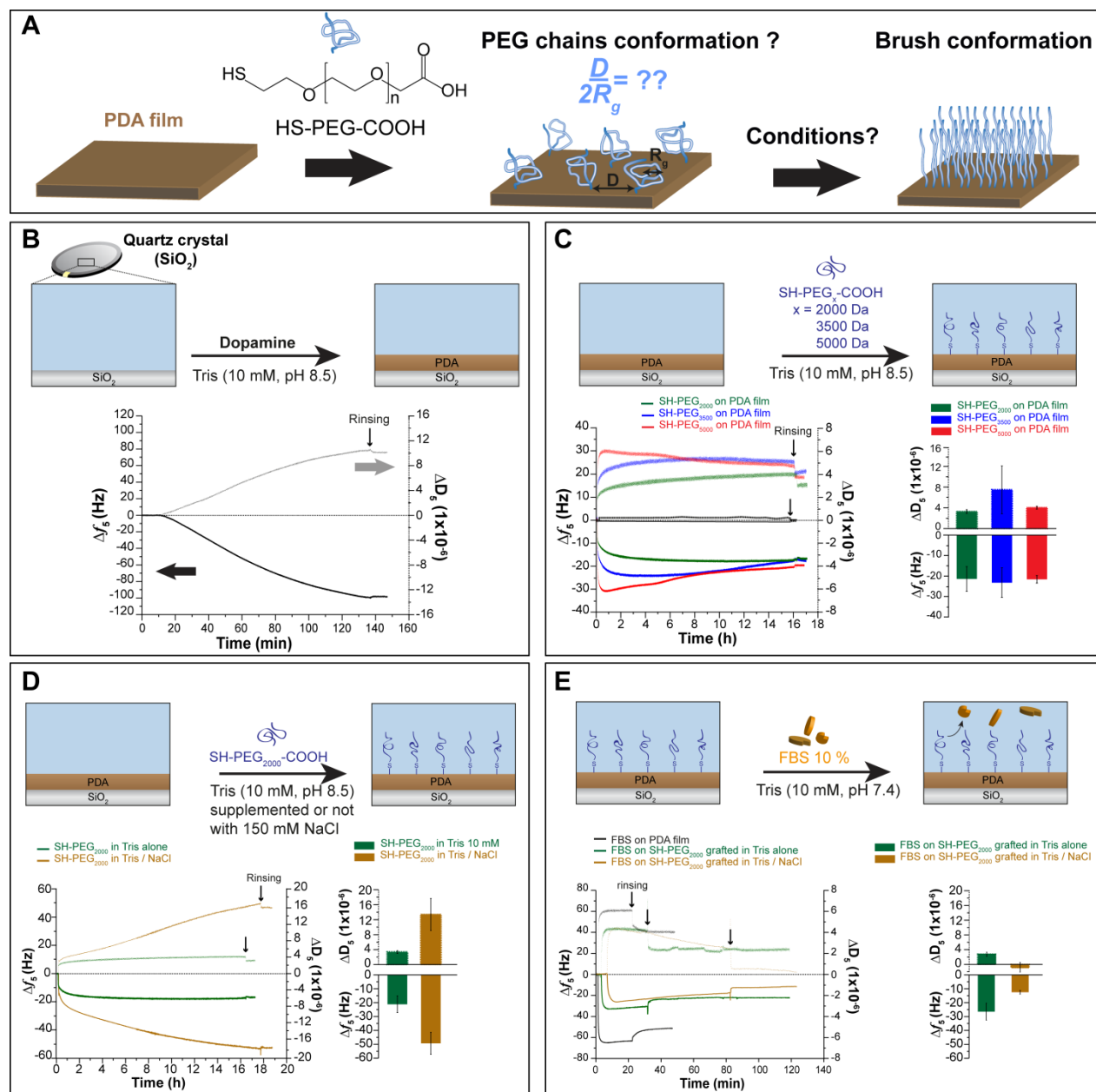


Figure 5. **A.** Scheme illustrating the PEGylation strategy of PDA film. **B.** Changes in resonant frequency Δf (black line) and dissipation ΔD (grey line) monitored at 25 MHz ($n = 5$) during formation of PDA adlayer on SiO₂ substrates. **C.** Left. Frequency (Δf_5) and dissipation (ΔD_5) shifts following the injection of SH-PEG_n-COOH with different molecular weights (Green: 2000 g/mol, Blue: 3500 g/mol and Red: 5000 g/mol) on PDA film. Right. Histograms illustrating the saturated frequency (Δf_5) and dissipation (ΔD_5) signals after rinsing with buffer. **D.** Left. Frequency (Δf_5) and dissipation (ΔD_5) shifts following the injection of SH-PEG₂₀₀₀-COOH in the absence of NaCl (Green) or in the presence of 150 mM of NaCl (Brown) on PDA film with the corresponding histograms after rinsing

with buffer. **E.** Left. Frequency (Δf_5) and dissipation (ΔD_5) shifts following the injection of FBS (10 vol%) on neat PDA film (Black), SH-PEG₂₀₀₀-COOH grafted on PDA in the absence (Green) or in the presence of 150 mM of NaCl (Brown) with the corresponding histograms after rinsing with buffer.

Layer	h (nm)	Δm (ng/cm ²)	ρ (kg/m ³)	η [mPa.s]	μ [MPa]	% H ₂ O
PDA	13.9±1.0	2754±103	1981±74	1.40±0.15	0.09± 0.014	4
PEG ₂₀₀₀	9.7±1.1	1650±462	1701±476	1.02±0.40	0.135±0.077	160

Table 3: Modeled parameters from QCM-D for the PDA film and the PEG₂₀₀₀ layer grafted in Tris buffer (10 mM, NaCl 150 mM, pH 8.5). %H₂O is the swelling percentage.

As for PDA film, we have determined the thickness of the adsorbed PEG layer by AFM nanoscratching experiments. The nanoscratching experiments performed on PDA-PEG films provided an increase of the thickness of 9.7±1.1 nm which corresponds to the attached PEG layer (Table 3, Figure S8). Such value is in good agreement with that obtained by Pop-Georgievski²⁰ for thiol terminated PEG brushes formed either on gold or PDA coated gold substrates using the melt approach. The determined thickness was thus used in order to achieve the fit of QCM-D data using the Kelvin-Voigt model. As depicted in Figure S9, the fitting profiles (black curves) were in excellent agreement with the measured data, yielding $\Delta m \sim 1650$ ng/cm² for the PEG layer. Moreover the shear modulus (μ_{PEG}), and shear viscosity (η_{PEG}) (Table 3 and Figure S10) are consistent with those obtained with hydrophilic polymer brushes⁶⁰⁻⁶¹. However, despite the good agreement between the experimental data and the applied Kelvin-Voigt model, the validation of the formation of PEG layer with high-surface density (i.e. polymer brush conformation) requires further investigation about the grafting density (σ), the distance (D) between the grafted polymers, the swelling degree of PEG chains as well as the overlap parameter ($D/2R_g$)^{20, 36} to determine the structural state of the bound chains. Therefore, by using the mass of the adsorbed PEG layer and its thickness determined by QCM-D and AFM nanoscratching experiments respectively, we could determine the overlap parameter. Moreover we have measured the

thicknesses of PDA and PDA-PEG layers in their dry states by AFM nanoscratching in order to calculate the swelling percentage ($\%_{\text{H}_2\text{O}}$) of each layer in Tris buffer (10mM, NaCl 150mM) which was found to be $\%_{\text{PDA-H}_2\text{O}} \sim 4 \%$ and $\%_{\text{PEG-H}_2\text{O}} \sim 160 \%$. These values are similar to those obtained in water by Pop-Georgievski et al.²⁰ using ellipsometry. The calculated value of $D/2R_g$ was equal to 0.1 which is lower than 0.5, ascertaining that the grafted PEG chains in these conditions are in brush conformation for which there is a significant chain overlap between the neighboring chains. It should be noted that higher salts concentrations (data not shown) have been also tried in order to improve the PEG grafting on PDA film, however similar frequency and dissipation shifts were measured which demonstrates that the surface was already saturated with PEG chains.

Protein repelling properties of PDA PEGylated substrates

Finally we performed series of QCM-D experiments in order to evaluate the protein repelling properties of the PEGylated PDA surfaces by injecting FBS solution at 10 % (vol%) in Tris buffer. Following the injection of FBS on PDA film (Figure 5E), the frequency decreases abruptly to reach a plateau with a frequency shift Δf_5 value of ~ -65 Hz with subsequent increase of the corresponding dissipation ($\Delta D_5 \sim 4 \times 10^{-6}$) indicating the absorption of viscous materials on the PDA surface. Furthermore, it is notable that both Δf and ΔD change only slightly after rinsing with Tris buffer indicating that proteins are strongly adsorbed on the PDA film. Compared to this latter, the PEGylated films formed in the absence (PDA-PEG₂₀₀₀) or presence of NaCl (PDA-PEG₂₀₀₀-NaCl) revealed lower Δf and ΔD shifts upon FBS injection which could be attributed to the lower effective mass of adsorbed proteins. Moreover, the behavior of the two films did not exhibit same kinetic absorption profiles for FBS. Indeed, while a plateau in the frequency and dissipation shifts is obtained after 10 min of FBS injection, the frequency shift Δf_5 monitored for

PDA-PEG₂₀₀₀-NaCl continued to increase monotonically with time suggesting that proteins are loosely attached in this condition. Moreover the residual frequency and dissipation shifts obtained after buffer rinsing with PDA-PEG₂₀₀₀-NaCl are reduced by a factor of 2 and 4 compared to the PDA-PEG₂₀₀₀ and PDA films respectively. However, Δf and ΔD did not come back to their initial levels after rinsing with Tris buffer indicating the presence of residual adsorbed proteins despite the presence of PEG brushes on the top of the PDA film. One possible explanation for this adsorption is the presence of defects in the PDA films. Similar effect has been observed by Emilson et al.²² despite the presence of polymer brushes on gold surfaces.

By using the optimized PEGylation conditions on PDA planar surfaces, we applied the same PEGylation strategy on PDA nanoparticles exhibiting a hydrodynamic diameter of ~140 nm. The PEGylation was thus achieved after overnight incubation of PDA NPs at a concentration of 1 mg/ml with 10 mg/ml of SH-PEG₂₀₀₀-COOH. The concentration of PEG herein was higher than that used in the case of planar surface in order to keep the same ratio as in the case of PDA planar surfaces. The PEGylation efficiency of PDA NPs was thus evaluated by measuring their hydrodynamic size, their Zeta potential by DLS and by investigating their chemical functionalities using Fourier-transform infrared spectroscopy (FTIR) on lyophilized NPs.

Buffer conditions	D_h (nm)	
	Ultrapure water	Tris buffer (10mM, NaCl 150mM, pH 7.4)
Bare PDA NPs	139 ± 2	764 ± 160
PEGylated PDA NPs	153 ± 2	147 ± 2

Table 4: Hydrodynamic diameters of bare PDA and PEGylated PDA NPs in Tris buffer in the absence and the presence of 150 mM of NaCl.

The hydrodynamic diameter of the freshly PEGylated PDA NPs measured in ultrapure water revealed an increase by 14 nm compared to the bare PDA NPs. Moreover the Zeta potential of the resulting NPs measured in the presence of 5mM of NaCl were not changed ($\zeta = -35 \pm 1$ mV) compared to the bare ones ($\zeta = -36 \pm 1$ mV). This could be related to the deprotonation of the carboxylic groups at the PEG extremities. Hence as the PDA NPs were already negatively charged, the deprotonation of PEG carboxylic groups would not induce a shielding of the PDA charges. Moreover, both nanoparticles types were stable for more than one month when stored at 4°C either in ultrapure water or in Tris buffer (10 mM, pH 7.4). However, when stored in the same buffer but in the presence of 150 mM NaCl to mimic the physiological ionic strength, only PEGylated PDA NPs remained stable as shown in the Table 4. Bare PDA NPs tend to form aggregates in the presence of NaCl with large precipitates in the solution (Table 4) within 24 hours of incubation. This demonstrates that the electrostatic repulsion between the bare PDA NPs was insufficient to maintain their colloidal stability in the presence of NaCl according to the DLVO theory⁶²⁻⁶³. In fact, the presence of salts will reduce the Debye screening length (κ^{-1}) which is given as κ^{-1} (nm) = $0.304/(I)^{0.5}$ (where I is the ionic concentration of monovalent ions in M). However, such problem was not observed in the case of PEGylated NPs where their stability is maintained by the PEG corona which acts as steric barrier. To further corroborate the PEGylation of the PDA NPs, they were lyophilized and characterized by Fourier-transform infrared spectroscopy (FTIR). As depicted in Figure S11, the FTIR spectrum of untreated PDA NPs exhibit a broad peak spanning from 3600 to 3200 cm^{-1} corresponding to the presence of OH groups and two other peaks at $\sim 1600 \text{ cm}^{-1}$ and $\sim 1500 \text{ cm}^{-1}$ characteristic of indole derivatives. This spectrum is in perfect agreement with the literature^{11, 14}. Added to these peaks, the PEGylated PDA nanoparticles showed characteristic spectral peaks of the PEG at 2880 cm^{-1}

(alkyl C-H stretching) and 1110 cm^{-1} (C-O-C stretching). These spectra are similar to those obtained by Ju et al.¹¹ indicating the efficiency of the PEGylation strategy.

Conclusion

In this work, we established for the first time, tightly controlled experimental conditions to synthesize and PEGylate PDA nanoparticles with well defined and reproducible physicochemical properties. As influencing factors on PDA NPs synthesis, we first studied the impact of [Ammonia]/[Dopamine] ratio and reaction temperature on their size and the yield. Our experimental data enabled the construction of surface response plots with accurate predictive values of the size and the yield of PDA NPs. The size, the zeta potential and the morphology of the synthesized NPs were further analyzed using DLS and AFM respectively. All of the nanoparticles were monodisperse and exhibited semi-spherical shapes with similar zeta potential values implying that they exposed the same chemical groups at their surfaces independently of their size. The nanomechanical properties of the covalently attached PDA NPs were studied by AFM nanoindentation experiments. It is noteworthy that the NPs Young's modulus decreased with their size, suggesting that PDA NPs with different sizes exhibit different geometric packing order of the oligomers/polymers in the core of NPs. Next, the PEGylation efficiency of PDA film with thiol-terminated PEG was monitored on solid substrates using QCM-D. The PEGylation strategy was optimized to graft the highest polymer density on the PDA film and to limit the non-specific adsorption of serum proteins by tuning the salts concentration in the solution. We have demonstrated the efficiency of our PEGylation strategy in the presence of salts even at low PEG concentrations. Finally, by transposing the same experimental conditions to PDA NPs, we could synthesize efficiently PEGylated NPs with high stability in physiological conditions as revealed by FTIR and DLS experiments respectively. Taken together, this work will provide more

standardized experimental conditions for the development of drug delivery platforms based on PDA with tunable physicochemical properties.

Acknowledgments

The authors are grateful to Dr Sylvain Trépout (Institut Curie, Orsay, France) for his contribution to cryoTEM experiments. IZ is thankful to the French Ministry of Research for the financial support of her PhD thesis.

References

1. A. C. Anselmo and S. Mitragotri, *Bioeng Transl Med*, 2016, **1**, 10-29.
2. V. J. Venditto and F. C. Szoka, Jr., *Adv Drug Deliv Rev*, 2013, **65**, 80-88.
3. J. C. Leroux, *Angew Chem Int Ed Engl*, 2017, **56**, 15170-15171.
4. E. Huynh and G. Zheng, *Wiley Interdiscip Rev Nanomed Nanobiotechnol*, 2013, **5**, 250-265.
5. Y. Liu, K. Ai, J. Liu, M. Deng, Y. He and L. Lu, *Advanced Materials*, 2013, **25**, 1353-1359.
6. P. Couvreur, in *Nanosciences and Nanotechnology: Evolution or Revolution?*, eds. J.-M. Lourtioz, M. Lahmani, C. Dupas-Haeberlin and P. Hesto, Springer International Publishing, Cham, 2016, pp. 253-272.
7. J. Massiot, V. Rosilio and A. Makky, *Journal of Materials Chemistry B*, 2019, **7**, 1805-1823.
8. H. Lee, S. M. Dellatore, W. M. Miller and P. B. Messersmith, *Science*, 2007, **318**, 426-430.
9. M. E. Lynge, R. van der Westen, A. Postma and B. Städler, *Nanoscale*, 2011, **3**, 4916-4928.
10. N. K. Kaushik, N. Kaushik, S. Pardeshi, J. G. Sharma, S. H. Lee and E. H. Choi, *Mar Drugs*, 2015, **13**, 6792-6817.
11. K.-Y. Ju, Y. Lee, S. Lee, S. B. Park and J.-K. Lee, *Biomacromolecules*, 2011, **12**, 625-632.
12. Y. Liu, K. Ai and L. Lu, *Chemical Reviews*, 2014, **114**, 5057-5115.
13. R. Mrówczyński, *Acs Appl Mater Inter*, 2018, **10**, 7541-7561.
14. C.-C. Ho and S.-J. Ding, *Journal of Materials Science: Materials in Medicine*, 2013, **24**, 2381-2390.
15. D. R. Amin, C. Sugnaux, K. H. A. Lau and P. B. Messersmith, *Biomimetics*, 2017, **2**, 17.
16. X. Jiang, Y. Wang and M. Li, *Sci Rep-Uk*, 2014, **4**, 6070.
17. Q. Ye, F. Zhou and W. Liu, *Chemical Society Reviews*, 2011, **40**, 4244-4258.
18. J. S. Suk, Q. Xu, N. Kim, J. Hanes and L. M. Ensign, *Advanced Drug Delivery Reviews*, 2016, **99**, 28-51.
19. R. Gref, Y. Minamitake, M. Peracchia, V. Trubetsky, V. Torchilin and R. Langer, *Science*, 1994, **263**, 1600-1603.
20. O. Pop-Georgievski, D. Verreault, M.-O. Diesner, V. Proks, S. Heissler, F. Rypáček and P. Koelsch, *Langmuir*, 2012, **28**, 14273-14283.
21. O. Pop-Georgievski, Š. Popelka, M. Houska, D. Chvostová, V. Proks and F. Rypáček, *Biomacromolecules*, 2011, **12**, 3232-3242.
22. G. Emilsson, R. L. Schoch, L. Feuz, F. Höök, R. Y. H. Lim and A. B. Dahlin, *Acs Appl Mater Inter*, 2015, **7**, 7505-7515.
23. W. Taylor and R. A. L. Jones, *Langmuir*, 2010, **26**, 13954-13958.
24. P. Kingshott, H. Thissen and H. J. Griesser, *Biomaterials*, 2002, **23**, 2043-2056.

25. D. Guo, G. Xie and J. Luo, *Journal of Physics D: Applied Physics*, 2013, **47**, 013001.
26. L. Sun, R. Riedel, S. G. Stanciu, F. Yang, N. Hampp, L. Xu and A. Wu, *Journal of Materials Chemistry B*, 2018, **6**, 2960-2971.
27. P. Guo, D. Liu, K. Subramanyam, B. Wang, J. Yang, J. Huang, D. T. Auguste and M. A. Moses, *Nature Communications*, 2018, **9**, 130.
28. X. Duan and Y. Li, *Small*, 2013, **9**, 1521-1532.
29. X. Zhang, C. Song, G. Ma and W. Wei, *Journal of Materials Chemistry B*, 2018, **6**, 7129-7143.
30. K. A. Beningo and Y.-I. Wang, *Journal of Cell Science*, 2002, **115**, 849-856.
31. M. Kaszuba, D. McKnight, M. T. Connah, F. K. McNeil-Watson and U. Nobbmann, *Journal of Nanoparticle Research*, 2008, **10**, 823-829.
32. A. Makky, P. Viel, S.-w. W. Chen, T. Berthelot, J.-L. Pellequer and J. Polesel-Maris, *Journal of Molecular Recognition*, 2013, **26**, 521-531.
33. J. L. Hutter and J. Bechhoefer, *Review of Scientific Instruments*, 1993, **64**, 1868-1873.
34. R. Lévy and M. Maaloum, *Nanotechnology*, 2001, **13**, 33-37.
35. M. V. Voinova, M. Rodahl, M. Jonson and B. Kasemo, *Physica Scripta*, 1999, **59**, 391-396.
36. J. L. Dalsin, L. Lin, S. Tosatti, J. Vörös, M. Textor and P. B. Messersmith, *Langmuir*, 2005, **21**, 640-646.
37. J.-M. Rabanel, P. Hildgen and X. Banquy, *Journal of Controlled Release*, 2014, **185**, 71-87.
38. J. Liebscher, R. Mrówczyński, H. A. Scheidt, C. Filip, N. D. Hädade, R. Turcu, A. Bende and S. Beck, *Langmuir*, 2013, **29**, 10539-10548.
39. D. R. Dreyer, D. J. Miller, B. D. Freeman, D. R. Paul and C. W. Bielawski, *Langmuir*, 2012, **28**, 6428-6435.
40. M. d'Ischia, A. Napolitano, V. Ball, C.-T. Chen and M. J. Buehler, *Accounts of Chemical Research*, 2014, **47**, 3541-3550.
41. N. F. Della Vecchia, R. Avolio, M. Alfè, M. E. Errico, A. Napolitano and M. d'Ischia, *Advanced Functional Materials*, 2013, **23**, 1331-1340.
42. S. Hong, Y. S. Na, S. Choi, I. T. Song, W. Y. Kim and H. Lee, *Advanced Functional Materials*, 2012, **22**, 4711-4717.
43. F. Bernsmann, O. Ersen, J.-C. Voegel, E. Jan, N. A. Kotov and V. Ball *ChemPhysChem*, 2010, **11**, 3299-3305.
44. W. Anderson, D. Kozak, V. A. Coleman, Å. K. Jämting and M. Trau, *J Colloid Interf Sci*, 2013, **405**, 322-330.
45. F. Varenne, A. Makky, M. Gaucher-Delmas, F. Violleau and C. Vauthier, *Pharm Res*, 2016, **33**, 1220-1234.
46. C. Cascio, D. Gilliland, F. Rossi, L. Calzolari and C. Contado, *Analytical Chemistry*, 2014, **86**, 12143-12151.
47. P. Eaton, P. Quaresma, C. Soares, C. Neves, M. P. de Almeida, E. Pereira and P. West, *Ultramicroscopy*, 2017, **182**, 179-190.
48. J. Stetefeld, S. A. McKenna and T. R. Patel, *Biophysical Reviews*, 2016, **8**, 409-427.
49. Q. Liu, B. Yu, W. Ye and F. Zhou, *Macromolecular Bioscience*, 2011, **11**, 1227-1234.
50. J. I. Kilpatrick, I. Revenko and B. J. Rodriguez, *Advanced Healthcare Materials*, 2015, **4**, 2456-2474.
51. D. Guo, J. Li, G. Xie, Y. Wang and J. Luo, *Langmuir*, 2014, **30**, 7206-7212.
52. K. Miyake, N. Satomi and S. Sasaki, *Appl Phys Lett*, 2006, **89**, 031925.
53. H. Hertz, *Journal für die Reine und Angewandte Mathematik*, 1881 **92**, 156-171.
54. K. L. Johnson, K. Kendall, A. D. Roberts and D. Tabor, *Proceedings of the Royal Society of London. A. Mathematical and Physical Sciences*, 1971, **324**, 301-313.
55. B. V. Derjaguin, V. M. Muller and Y. P. Toporov, *J Colloid Interf Sci*, 1975, **53**, 314-326.

56. K. K. Sweers, M. L. Bennink and V. Subramaniam, *J Phys Condens Matter*, 2012, **24**, 243101.
57. G. Smolyakov, C. Formosa-Dague, C. Severac, R. E. Duval and E. Dague, *Micron*, 2016, **85**, 8-14.
58. L. Chopinet, C. Formosa, M. P. Rols, R. E. Duval and E. Dague, *Micron*, 2013, **48**, 26-33.
59. K.-Y. Ju, M. C. Fischer and W. S. Warren, *ACS Nano*, 2018, **12**, 12050-12061.
60. G. Liu and G. Zhang, *The Journal of Physical Chemistry B*, 2008, **112**, 10137-10141.
61. A. Saftics, G. A. Prósz, B. Türk, B. Peter, S. Kurunczi and R. Horvath, *Sci Rep-Uk*, 2018, **8**, 11840.
62. B. Derjaguin and L. Landau, *Progress in Surface Science*, 1993, **43**, 30-59.
63. E. J. W. Verwey, *The Journal of Physical and Colloid Chemistry*, 1947, **51**, 631-636.